RMetS
Royal Meteorological Society

The effect of indiscriminate nudging time on large and small scales in regional climate modelling: Application to the Mediterranean basin

Tamara Salameh,*Philippe Drobinski and Thomas Dubos
Institut Pierre Simon Laplace/Laboratoire de Météorologie Dynamique, École Polytechnique/ENS/UPMC/CNRS, Palaiseau, France
*Correspondence to: T. Salameh, Institut Pierre Simon Laplace/ Laboratoire de Météorologie Dynamique, École Polytechnique, F-91128, Palaiseau Cédex, France. E-mail: tamara.salameh@lmd.polytechnique.fr

A regional climate model (RCM) is driven by the ERA-40 reanalyses produced by the ECMWF general circulation model (GCM) to simulate the winter 1998 climate over the Mediterranean basin. In this article, we consider the effects on internal variability of temporal nudging. This technique consists of relaxing the RCM's prognostic variables towards the GCM values within a predetermined time-scale, with the aim of disallowing large and unrealistic departures between driving and driven fields. To interpret the significant effect of time nudging on the regional climate prediction, we develop a 'toy model' basically consisting of resolving a linear transport equation with a Newtonian relaxation term. This model predicts the existence of an optimal nudging time which depends on the time-scale over which numerical errors affect significantly the accuracy of the 'regional' solution at the large spatial scales, and the typical time-scale of the small-scale phenomena that are not resolved by the GCM. Copyright © 2010 Royal Meteorological Society

Key Words: downscaling; uncertainties; large/small-scale perturbations; potential vorticity

Received 25 January 2008; Revised 24 July 2009; Accepted 9 September 2009; Published online in Wiley InterScience 19 January 2010

Citation: Salameh T, Drobinski P, Dubos T. 2010. The effect of indiscriminate nudging time on large and small scales in regional climate modelling: Application to the Mediterranean basin. *Q. J. R. Meteorol. Soc.* **136**: 170–182. DOI:10.1002/qj.518

1. Introduction

Climate varies across a wide range of temporal and spatial scales. Yet climate modelling has long been approached using global general circulation models (GCMs) that can resolve only the broader scales of atmospheric circulations (around 100 km grid resolution). Clearly, large-scale climate determines the environment for mesoscale and microscale processes that govern the weather and local climate, but, likewise, processes that occur at the regional scale may have significant impacts on the large-scale circulation. Resolving such interactions will lead to much improved understanding of how climate both influences, and is influenced by, human activities.

Hence there is a need to develop tools for downscaling GCM predictions to generate finer-scale projections of local climatologies. Downscaling is the process of deriving regional climate information based on large-scale climate conditions. Both dynamical and statistical downscaling methods have been used extensively in the last decade to produce regional climate (Wilby and Wigley, 1997, provide a review).

Statistical downscaling is a method for obtaining high-resolution climate from GCMs by deriving statistical relationships between observed small-scale (often station-level) variables and larger (GCM)-scale variables, using either analogue methods (circulation typing), regression analysis, or neural network methods (Wilby and Wigley, 1997; Wilby *et al.*, 1998). Statistical downscaling may be used whenever suitable small-scale observed data are available to derive the statistical relationships (e.g. Salameh *et al.*, 2009).

Dynamical downscaling consists of driving a regional climate model (RCM) by a GCM over an area of interest since decreasing grid spacing in mesoscale models generally improves the realism of the results (Mass *et al.*, 2002). This nesting technique can be one-way, so the circulations produced by the RCM do not feed back into the GCM, or two-way (Giorgi, 1990). Previous studies have investigated the sensitivity of the RCM predictions to initial and boundary conditions, frequency of update of boundary conditions, size and resolution of the domain of simulation, spin-up time, and physical parametrisations, in order to prevent these models misleading (Bhaskaran *et al.*, 1996; Seth and Giorgi, 1998; Noguer *et al.*, 1998; Laprise *et al.*, 2000; Denis *et al.*, 2002, 2003). For long-term RCM modelling, Qian *et al.* (2003), Žagar *et al.* (2006), and Lo *et al.* (2008) showed that RCM simulations re-initialized periodically have better results than continuous runs. However re-initialization creates discontinuities which are detrimental for time variability studies. All these studies have shown that RCM internal variability may be very complex and that its impact on regional climate predictions is far from negligible. One way to overcome this problem is to consider the effects on internal variability of large-scale nudging, which is a technique originally developed for assimilation issues (Davies and Turner, 1977; Schraff, 1997; Li *et al.*, 1998; Vidar *et al.*, 2003) but increasingly popular to drive RCMs. This technique consists of partially imposing the large scale of the driving fields on the RCM simulation with the aim of disallowing large and unrealistic departures between driving and driven fields. Two different types of nudging exist, both requiring constant adjustments: spectral nudging which consists of driving the RCM on selected spatial scales (e.g. Von Storch *et al.*, 2000) and temporal nudging or Newtonian relaxation, which consists of relaxing the RCM's prognostic variables towards the GCM values within a predetermined relaxation time. For the latter, the smaller the nudging time, the closer are the RCM predictions to the GCM's fields interpolated on the RCM grid and the larger is the inhibition of the RCM physics. Spectral nudging is indeed a solution to the undesirable effect of nudging on small scales and allows us to overcome the issue of indiscriminate temporal nudging, but indiscriminate nudging is suited for basic irregularly spaced data assimilation. This appropriate solution of basic data assimilation contributes to widely spread the indiscriminate nudging option in many up-to-date regional numerical models such as MM5 (Grell *et al.*, 1993), WRF (Skamarock *et al.*, 2005), Méso-NH (Lafore *et al.*, 1998), RAMS (Pielke *et al.*, 1992), and LMDZ (Genthon *et al.*, 2002). The use of indiscriminate nudging is thus widely used for applications such as data assimilation and dynamical downscaling. For this reason, it is useful to assess the various error sources and how they scale with the indiscriminate nudging time, which is the main aim of the present work.

In this paper, we analyze the impact of large-scale nudging on RCM internal variability. To investigate the effect of time nudging on the regional climate prediction, we develop a 'toy model' basically consisting of resolving a linear transport equation with a Newtonian relaxation term. This model allows the identification of the different sources of errors in the RCM, the evaluation of the time-scale over which numerical errors affect significantly the accuracy of the RCM solution at the large spatial scales, and the time-scale of the small-scale phenomena that are not resolved by the GCM. We then use the results obtained with the linear model to interpret a series of numerical experiments conducted with the fifth-generation Penn State/NCAR mesoscale model MM5 as the RCM and performed with different nudging times over the Mediterranean basin. The RCM is nudged towards the reanalyses (ERA-40) of the European Centre for Medium-Range Weather Forecasts (ECMWF) of November and December 1998. Despite the wide complexity gap between the two models, their combined analyzes allows a better insight into the effects of indiscriminate nudging on the different scales in regional modelling and in the determination of an appropriate nudging time.

After the introduction in section 1, section 2 describes the 'toy model' which consists of a linear one-dimensional transport equation with a Newtonian relaxation term. Section 3 details the RCM used in this study and describes the RCM internal variability as a function of large-scale nudging. Section 4 gives an interpretation of the RCM results in the light of the 'toy model' learnings. Finally section 5 concludes the study and points out some open research questions needing further investigation.

2. The toy model

2.1. *Rationale*

Finding the optimal nudging time for a realistic nonlinear model is in general a nonlinear optimization problem. Iterative techniques based on adjoint methods can be used to obtain an accurate and quantitative estimate of the optimal time. However this is an expensive task which must be done for each specific model and configuration. The result also depends on the criterion to be optimized (the cost function). The main objective of the present work is not to obtain the optimal value of the nudging time or to propose a new general method to quantitatively estimate the optimal nudging time in realistic models. Our aim is to gain a general insight into the key mechanisms involved in the impact of indiscriminate nudging on the large scales and the small scales of a regional climate simulation.

To do so, we develop a toy model amenable to analytical treatment, which contains enough ingredients to suffer from the same drift phenomenon as a complex atmospheric model and needs to be guided as well. As soon as the toy model presents a variety of spatial scales, the issue of the degradation of the small scales by indiscriminate nudging arises. Since the nudging technique is of very general applicability, independently of the underlying dynamics, the adequacy of the toy model to study the influence of the nudging time on regional climate simulations does not result from its approximating a real-world model but from the key ingredients the toy model contains: a variety of scales and a tendency to drift away from the large-scale situation. The approach of analyzing complex models by resorting to synthetic models containing a few key ingredients with only a formal similarity with the original problem has a long history and has proven useful in the past. Actually Waldron *et al.* (1996) use a linear wave model in order to compare the impact of indiscriminate and spectral nudging at the small and large scales, before turning to a realistic model. The approach used in this paper is quite similar.

2.2. *Setting*

The basic parameters and scales defining an optimal nudging time appear better in a simplified problem. Because most dynamical variables evolve under the combined effect of transport and various sources, the toy model we consider consists of a one-dimensional transport equation

$$\frac{\partial q}{\partial t} + \overline{U}\frac{\partial q}{\partial x} = s(x)\,, \tag{1}$$

where $\overline{U}$ is a constant, uniform velocity and the right-hand-side $s(x)$ represents non-conservative effects, assumed here time-independent for simplicity. One can think for instance of the transported variable q as being Ertel's potential vorticity $(2\Omega + \nabla \times V) \cdot \nabla\theta/\rho$, where ρ is the air density, Ω is the angular velocity vector of the Earth's rotation, V is the air velocity and θ is the potential temperature. Potential vorticity is a conservative variable obeying a conservation equation of transport similar to Eq. (1). The right-hand side then corresponds to the sources of potential vorticity due to dissipation, notably over mountains and valleys. Because of its extreme simplicity, Eq. (1) admits a closed-form general solution:

$$q(x,t) = q_0(x - \overline{U}t) + q_{ss}(x) \tag{2}$$

where q_0 is an arbitrary transient and q_{ss} is the steady response to the forcing:

$$\overline{U}\frac{\partial q_{ss}}{\partial x} = s(x). \tag{3}$$

The subscript $_{ss}$ stands for 'small-scale', due to the assumed small-scale nature of the forcings.

We now introduce two imperfect models which try to numerically approach the solution of Eq. (1). The first one is our toy analogue of a GCM and has insufficient resolution to resolve the small-scale source s, hence:

$$\frac{\partial q_{ls}}{\partial t} + \overline{U}\frac{\partial q_{ls}}{\partial x} = 0\,, \tag{4}$$

where the subscript $_{ls}$ stands for 'large-scale'. We assume that the lack of a proper representation of the small-scale sources is the main source of error in q_{ls}, effectively neglecting discretization error, imperfect initialization, etc. As a result:

$$q_{ls} = q_0(x - \overline{U}t)\,, \tag{5}$$

where q_0 is the transient that effectively occurs in the perfect physical model described by Eq. (1). Obviously, the small-scale details that occur in response to the sources s are missing from the field q_{ls}. We finally introduce a 'regional' model, resolving Eq. (1) with improved resolution over a limited interval. Because spatial and temporal discretizations introduce errors, the numerical model effectively solves an equation slightly different from Eq. (1), and which includes numerical diffusion or dispersion. In order to compensate for the accumulated numerical errors, a non-physical nudging term is added which keeps the 'regional' solution not too far from the large-scale solution q_{ls}:

$$\frac{\partial q_r}{\partial t} + \overline{U}\frac{\partial q_r}{\partial x} = \overline{U}\frac{\partial q_{ss}}{\partial x} - \frac{1}{\tau}(q_r - q_{ls}) + K_{num}\frac{\partial^2 q_r}{\partial x^2}, \tag{6}$$

where K_{num} is the numerical diffusion (we do not consider here numerical dispersion) and the nudging time τ is a freely tunable parameter. The shorter the time τ, the closer q_r will be to q_{ls}, and hence the less accurate the small scales of q_r will be. In the following subsection, we determine quantitatively the dependance on τ of the accumulation of numerical errors, which occurs for long nudging times, and of the damping of the small scales, which occurs for short nudging times. The best compromise between these two sources of errors defines an optimal nudging time, which can be explicitly derived for this toy model.

2.3. *Error estimate and optimal nudging time*

In order to estimate the effect of the nudging time on the regional solution q_r and the errors made at large and small scales, we now analyze Eq. (6) in Fourier space. The regional solution q_r differs from the ideal solution by a large-scale contribution proportional to q_{ls} and a small-scale contribution proportional to q_{ss} (see Appendix). This provides a bound on the r.m.s error ϵ:

$$\epsilon \le \epsilon_{ls} + \epsilon_{ss} \tag{7}$$

Given characteristic scales $L_{ls} \gg L_{ss}$, corresponding to wave numbers $k_{ls} \ll k_{ss}$, of the functions q_{ls} and q_{ss}, we obtain the estimates

$$\epsilon_{ls} \sim \|\widehat{q}_{ls}\| \left|\frac{1}{1 + K_{num}k_{ls}^2\tau} - 1\right|, \tag{8}$$

$$\epsilon_{ss} \sim \|\widehat{q}_{ss}\| \left|\frac{1}{1 + \left(\mathrm{i}\tau\overline{U}k_{ss}\right)^{-1}} - 1\right|. \tag{9}$$

Details on the calculation of error estimate are developed in the Appendix.

Two time-scales associated with two asymptotic regimes appear in the expressions for ϵ_{ls} and ϵ_{ss}. The first time-scale is $\tau_{num} = \left(K_{num}k_{ls}^2\right)^{-1} \sim L_{ls}^2/K_{num}$, the time-scale over which numerical errors affect significantly the accuracy of the 'regional' solution at spatial scale k_{ls}. The second time-scale is $\tau_{ss} = \left(\overline{U}k_{ss}\right)^{-1}$, the typical time-scale of the small-scale phenomena that are not resolved by the GCM. In the limit where $\tau \ll \tau_{num}$,

$$\epsilon_{ls} \sim \|\widehat{q}_{ls}\| \left|\frac{1}{1 + K_{num}k_{ls}^2\tau} - 1\right| \sim \|\widehat{q}_{ls}\| \frac{\tau}{\tau_{num}}, \tag{10}$$

while if $\tau \gg \tau_{ss}$,

$$\epsilon_{ss} \sim \|\widehat{q}_{ss}\| \frac{\tau_{ss}}{\tau}. \tag{11}$$

We can expect that $\tau_{num} \gg \tau_{ss}$, i.e. it takes much longer for the noise to contaminate the large scales than for the small scales to evolve under their own dynamics. Hence there exists a range where $\tau_{ss} \ll \tau \ll \tau_{num}$ and

$$\epsilon_{ls} + \epsilon_{ss} \sim \|\widehat{q}_{ls}\| K_{num}k_{ls}^2\tau + \|\widehat{q}_{ss}\| \left(\tau\overline{U}k_{ss}\right)^{-1}. \tag{12}$$

This estimate of the error attains a minimum for

$$\tau_{opt} \sim \sqrt{\frac{\|\widehat{q}_{ss}\|}{\|\widehat{q}_{ls}\|}}\sqrt{\tau_{num}\tau_{ss}}\,. \tag{13}$$

This result emphasizes the effects which contribute to the total error committed by the nudged simulation: the damping of small scales if τ is much smaller than the dynamical time-scale τ_{ss}, and the deviation of large scales from the reanalyses if τ is much larger than the time-scale τ_{num}. Both sources of error can be kept small if $\tau_{ss} \ll \tau_{num}$ with an optimum nudging time given by Eq. (13).

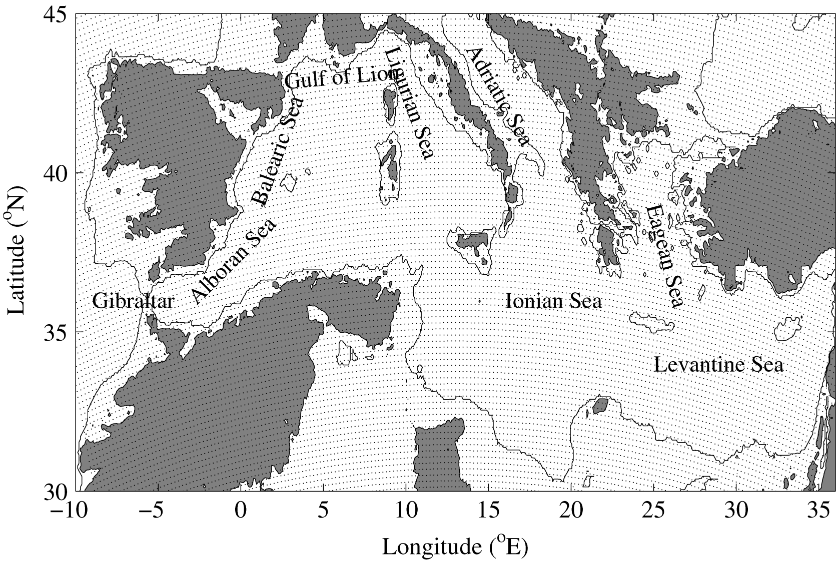

Figure 1. The MM5 RCM domain; solid lines indicate the coasts, grey areas represent topography higher than 500 m and the dots represent the nodes of the horizontal grid.

3. Mediterranean climate modelling

3.1. Numerical model

The RCM used to conduct the simulations is the fifth generation Penn State–National Center for Atmospheric Research RCM, MM5 version 3.6 (Dudhia, 1993; Grell *et al.*, 1993). The model solves the non-hydrostatic equations of motion in a terrain-following sigma coordinates. The domain covers the Mediterranean basin (Figure 1).

It is centred on 38°N, 13°E and covers an area of 4000 km × 1150 km. The horizontal resolution is 21 km and 37 unevenly spaced full sigma levels are used. The lowermost half-sigma level ($\sigma = 0.999$) is about 12 m above ground. The vertical distance between the model levels is about 50 m close to the ground and increases up to 1200 m near the upper boundary which is located at 100 hPa. The model orography is interpolated from terrain data with 30″ resolution. It is filtered by a two-pass smoother–desmoother (Guo and Chen, 1994) in order to remove two-grid-interval waves that would induce numerical noise. Information on land use was obtained from United States Geological Survey (USGS) data with the same horizontal resolution as for orography. The simulations use up-to-date local land surface characteristics coupled with the advanced land surface model (NOAH-LSM) (Chen and Dudhia, 2001). A complete set of physics parametrisations is used. The cloud microphysics are treated with a sophisticated scheme having prognostic equations for cloud water, cloud ice, cloud ice particle number concentration, rain, snow and graupel (Reisner *et al.*, 1998). The Grell cumulus parametrisation (Grell, 1993) is used. The radiation scheme accounts for the interaction with moisture and clouds (Grell *et al.*, 1993; Mlawer *et al.*, 1997). The atmospheric boundary layer is parametrised using the Hong and Pan scheme (Hong and Pan, 1996). It is an efficient scheme based on the Troen and Mahrt representation of the countergradient term and eddy viscosity profile in the well-mixed atmospheric boundary layer.

The GCM outputs are the ECMWF reanalyses ERA-40 which are available every six hours on a 1.125° × 1.125° latitude–longitude grid. Since the interpolation routine of the MM5 modelling system needs pressure level data, the standard-level-pressure version of the ECMWF data is used.

In this paper, we analyze the impact of large-scale nudging on RCM internal variability based on a series of numerical experiments performed with different nudging times over the Mediterranean basin. The nudging time τ ranges between 0 h (basically the ERA-40 fields interpolated onto the RCM grid) and 10 d ($\tau = 1, 2, 3, 4, 5, 6, 12$ h, and 1, 2, 5 and 10 d). One simulation is performed without nudging (i.e. $\tau = \infty$). Nudging is applied on the 3D GCM fields (wind, temperature and humidity) as proposed by Lo *et al.* (2008). All the simulations start on 1 November 1998 and end on 31 December 1998.

3.2. Results

The Mediterranean basin presents several characteristics. First, because of the latitudes that it covers, it is a transition area under the influence of both midlatitude and tropical variability: to the north, a large part of the atmospheric variability is linked to the North Atlantic Oscillation (NAO) and other midlatitude teleconnection patterns (Xoplaki, 2002; Trigo *et al.*, 2004), while the southern part of the region is under the influence of the descending branch of the Hadley cell materialized through the Azores High, with in addition El Niño Southern Oscillation (ENSO) influence to the east (Rodwell and Hoskins, 1996; Price *et al.*, 1998). At the southern limit of the North Atlantic storm tracks, the Western Mediterranean region is particularly sensitive to interannual displacement of the trajectories of midlatitude cyclones that can modulate the precipitation over the region mainly during the winter season when the impact of the NAO is greatest (Rodriguez-Fonseca and De Castro, 2002). The Mediterranean climate is also influenced by tropical and subtropical systems, such as ENSO, tropical cyclones, Saharan dust and the South Asian monsoon (Rodó *et al.*, 1997; Reale *et al.*, 2001; Rodó, 2001; Mariotti *et al.*, 2002).

At finer scale, Mediterranean region features a nearly closed sea with high sea surface temperature during summer and autumn surrounded by an almost continuous barrier of

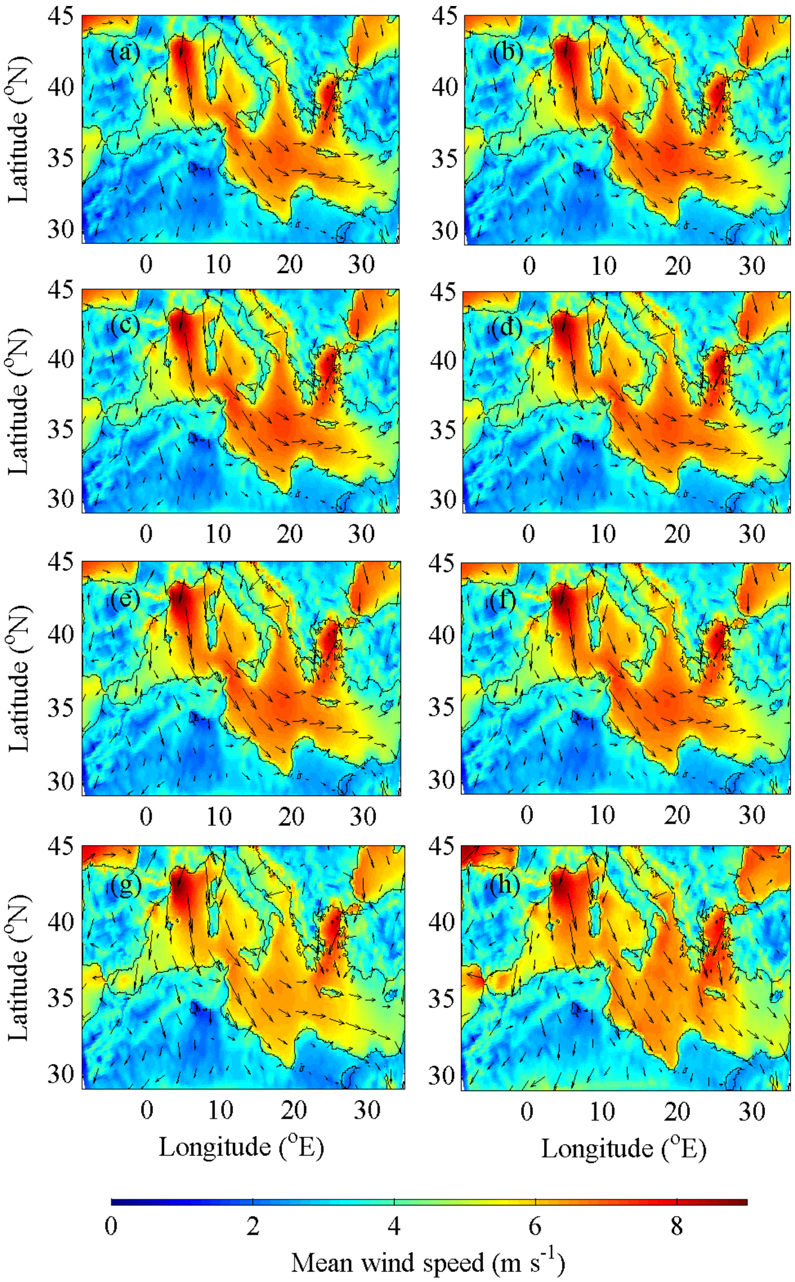

Figure 2. 3-hourly surface wind speed (shading) and direction (arrows) averaged over November and December 1998 for nudging time τ equal to (a) 1 h, (b) 2 h, (c) 3 h, (d) 4 h, (e) 5 h, (f) 6 h, (g) 12 h and (h) ∞ (no nudging). This figure is available in colour online at www.interscience.wiley.com/journal/qj

mountains. The complex topography plays a crucial role in steering air flow and the Mediterranean Sea acts as a moisture and heat reservoir, so that energetic mesoscale features are present in the atmospheric circulation which can evolve to high-impact weather systems such as heavy precipitation and wind storms. The ability to predict such high-impact weather events, their impacts and their evolution in the context of climate change is still low because of the contribution of fine-scale processes. Figure 2 displays the mean surface wind field averaged over November and December 1998, when teleconnections with synoptic-scale atmospheric circulation is the greatest (e.g. Dünkeloh and Jacobeit, 2003). The different panels of Figure 2 correspond to different nudging times (τ ranging from 1 to 12 h, the last panel corresponding to the simulation performed without nudging).

On average, the mean surface wind field is not strongly affected by the nudging and the typical wind regimes in the various sub-basins can be identified. In the Alboran Sea (the westernmost Mediterranean), the levanter blows from the east and in winter it may be strong and long lasting (up to 10 days). In the central Mediterranean, the north-north-west cold and dry mistral (e.g. Jansá 1987; Jiang *et al.*, 2003; Caccia *et al.*, 2004; Corsmeier *et al.*, 2005; Drobinski *et al.*, 2005; Guénard *et al.*, 2005, 2006; Lebeaupin Brossier and Drobinski, 2009) and its companion wind the tramontane (e.g. Drobinski *et al.*, 2001) blows in the Gulf of Lion, occasionally up to the African coasts (Salameh *et al.*, 2007). Winter 1998 was a period of particularly frequent and intense mistral events. The northeasterly strong and cold bora (Yoshino, 1976; Jurčec, 1981; Smith, 1987; Pandžić and Likso, 2005) affects the entire Adriatic Sea and bora-type winds are also visible in the northern Aegean Sea. In the Levantine basin, the prevailing winds are the etesians (Ziv *et al.*, 2004) whereas the Black Sea is dominated by northerly winds (Efimov and Shokurov, 2002); a cyclonic circulation dominates the eastern part of the basin, while an anticyclonic circulation prevails on its western side. In detail, significant differences can be seen between the different simulations: in the region of the Gibraltar Strait over the Alboran Sea, the levanter is nearly non-existent in the case of strong nudging ($\tau < 6$ h; Figure 2(a–f)), whereas it can blow on average up to 6–7 m s^{-1} when nudging is applied on longer time-scales ($\tau \geq 12$ h; Figure 2(g–h)). Over the Gulf of Lion, the footprint of the mistral and tramontane jets spreads westwards over a wider zone and eastwards to the Ligurian Sea when τ increases. In the central basin, surface wind speed decreases with increasing τ and the etesians veer from the west ($\tau < 6$ h) to the northwest ($\tau \geq 12$ h), in better agreement with the climatology by Zecchetto and De Biasio (2007). Other less significant differences are visible with winds intensifying over the Adriatic Sea and over the southern shore of the Black Sea with increasing τ.

Compared to the mean surface wind field, the variability in strength and direction is even more sensitive to the nudging time. Following Zecchetto and De Biasio (2007), we define the wind steadiness S (i.e. indicating the variability of the wind direction) and the relative wind speed G (i.e. indicating the variability of the wind speed) as

$$\begin{aligned} S &= \frac{100}{\overline{U}}\left(\overline{u}^2+\overline{v}^2\right)^{1/2}, \\ G &= \frac{\sigma_U}{\overline{U}}. \end{aligned} \tag{14}$$

where U is the surface wind speed of components u and v, σ_U is the standard deviation of the wind speed and the overbar denotes time averaging. The larger the variability in wind direction and wind speed, the weaker is the wind steadiness S and the stronger is the relative wind speed G, respectively. The wind variability differs in the eastern and western Mediterranean sub-basins and are strongly dependent on the nudging time as displayed in Figures. 3 and 4.

The wind steadiness field (Figure 3) defines the extent of the main Mediterranean wind systems well but varies significantly with time nudging. For $\tau \leq 6$ h, the highly steady etesians ($S > 65$) in the Levantine basin affect an area roughly east of 24°E as shown in Zecchetto and De Biasio (2007) between 2000 and 2004. However, when $\tau \geq 12$ h, wind steadiness decreases to values $S \simeq 50$ over a much less defined area in the absence of nudging. However, the sensitivity of the etesians to time nudging is weak compared to the sensitivity of the mistral/tramontane wind systems in the Gulf of Lion. West of 12°E, two zones of large steadiness ($S > 65$) over the Gulf of Lion and off the coasts of Tunisia are clearly detached for $\tau \leq 1$ h and $\tau \geq 12$ h whereas when $1\,\text{h} \leq \tau \leq 12$ h, these two regions of large steadiness merge into one. Similarly to the Levantine basin, wind steadiness decreases with increasing τ and $\tau \geq 12$ h. Contrary to Zecchetto and De Biasio (2007) climatology, the western Mediterranean basin in winter 1998 is characterized by large steadiness ($S > 65$ in 1998 compared to $S < 60$ on average for winters 2000 to 2004). This can reasonably be explained by the unusual high frequency of intense mistral/tramontane events. Finally, the regions of very low wind steadiness ($S < 40$) are consistent with the Zecchetto and De Biasio (2007) climatology, whatever the nudging time τ, except for the Sicilian Channel ($S > 55$ in 1998 compared to $S < 40$ on average for winters 2000 to 2004): they are the Alboran, Balearic, Adriatic, Tyrrhenian and Black Seas. The fact that, in general, wind steadiness decreases is consistent with the fact that the production of small-scale wind structures is favoured by the absence of relaxation to the GCM wind field.

The relative wind speed variability (Figure 4) shows that, as in Zecchetto and De Biasio (2007) climatology, the highest values ($G > 0.40$) occur in areas swept by winds from land, such as the Gulf of Lion, and the Alboran, Adriatic, and Aegean Seas, as well as at the lee side of Corsica and Sardinia in the northern Tyrrhenian Sea, and Crete and Rhodes in the Levantine basin, indicating strong airflow–orography interactions. The lowest values of relative wind speed variability ($G < 0.40$) are found in the southernmost part of the basin (below about 35°N), offshore from flat coastal areas that mainly experience winds from the sea. The relative wind speed G in this region is extremely sensitive to the nudging time τ. Indeed, over the Ionian and Levantine basins, G decreases when τ increases up to 1 h. The G field varies very little up to $\tau = 12$ h and then increases significantly with increasing τ. Contrary to Zecchetto and De Biasio (2007), the highest values of G does not occur in the Gulf of Lion because of the more frequent occurrence of strong mistral/tramontane events (even though G is still high with values exceeding 0.5 in the worst case) but in the Alboran Sea. The high wind speed variability confirms the presence of orographic effects, which is evident along the coast of the Gulf of Lion and Adriatic Sea, as an effect of the funnelling of the northwesterly mistral/tramontane and northeasterly bora through the chain gaps, but is also relevant east of Sardinia–Corsica and south of Crete–Rhodes.

As for the wind steadiness S, the fact that on average G increases with τ is consistent with the simulation of small-scale features. In the absence of nudging, the G pattern does not show zones as distinct as in the presence of nudging.

Finally, the significant impact of the nudging time on the mean surface wind and its variability affects dramatically the accumulated precipitation pattern in intensity and location and, to a lesser extent, the surface temperature field (not shown). The question is thus: can we determine from the RCM fields an optimal nudging time minimizing the error made on the large-scale field, and simultaneously allowing the production of realistic fine-scale structures contributing significantly to the climate of the region?

4. Discussion

In this section,we assess to what extent the toy model can help interpret the dependence of the MM5 simulations on the nudging time τ. Specifically, we attempt to estimate small-scale and large-scale times τ_{num} and τ_{ls} from our set of MM5 simulations.

For this purpose, we choose $q = PV$, because it is a conservative variable verifying a conservation equation similar to Eq. (1) and because the complex orography of our domain is a source of small-scale potential vorticity. Indeed, when low-level flow splitting or wave breaking occurs, dissipative processes in the turbulent regions generate PV that streams downwind in ‘PV banners’ (e.g. Smith, 1989; Smith *et al.*, 2007). For instance, the mistral is qualified as a primary PV banner (Drobinski *et al.*, 2005; Guénard *et al.*, 2006), contrary to smaller streams of vorticity which

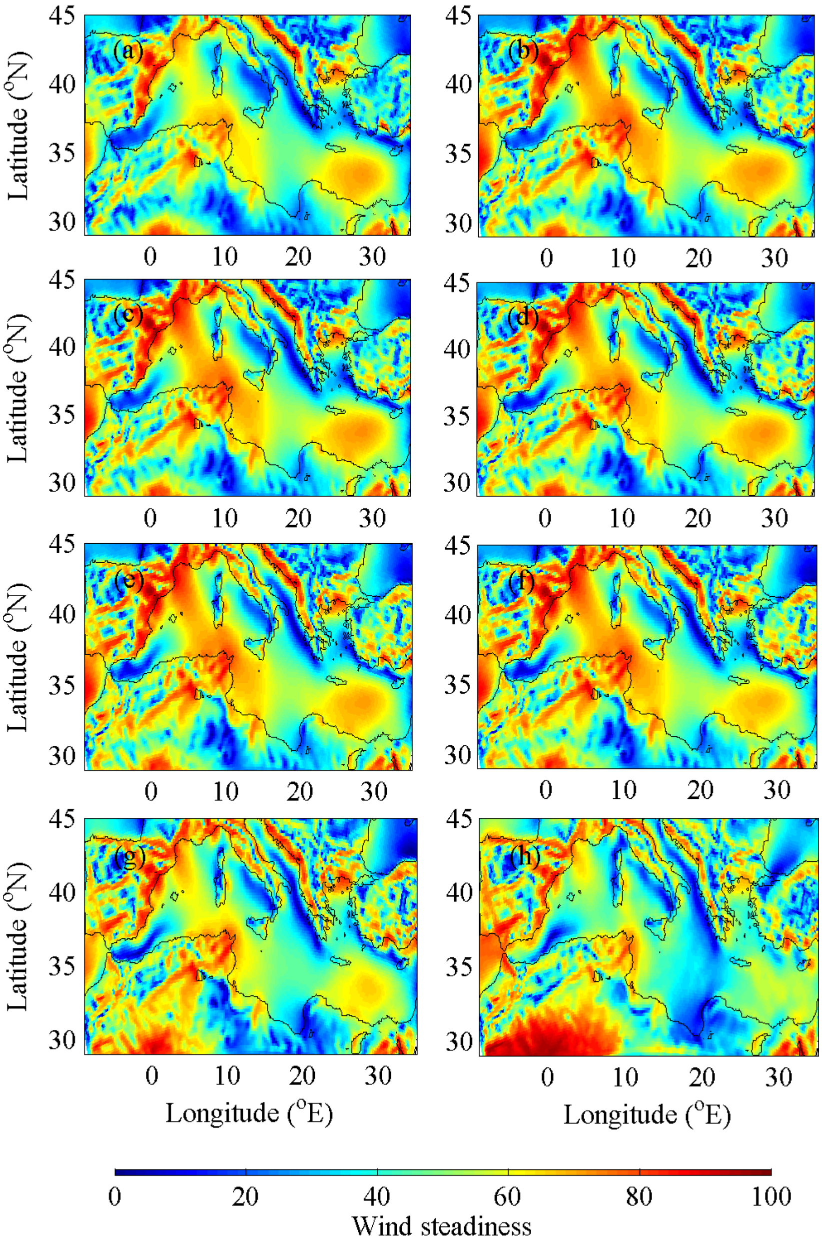

Figure 3. Surface wind steadiness S over November and December 1998 for nudging time τ equal to (a) 1 h, (b) 2 h, (c) 3 h, (d) 4 h, (e) 5 h, (f) 6 h, (g) 12 h and (h) ∞ (no nudging). This figure is available in colour online at www.interscience.wiley.com/journal/qj

wrap up into pairs of eddies of opposite signs due to the irregular peak and pass structure of the mountain ridges forming eventually multiple PV banners (Aebischer and Schär, 1998; Schär *et al.*, 2003; Flamant *et al.*, 2004). Figure 5 displays the 850 hPa PV fields for the various values of τ for day 20 of the two-month simulation. As for the mean surface wind field and wind variability, the PV field is very sensitive to the nudging time. The major source of PV, present in all simulations, is the mistral (generating positive PV)/tramontane (generating negative PV) winds, shooting through the Rhône and Aude valley gaps between the Alps and the Pyrenees, and bounded on both sides by mountain-induced PV banners shed from major peaks in the Pyrenees, the Massif Central and the Alps (Jiang *et al.*, 2003; Drobinski *et al.*, 2005). When τ increases, smaller-scale PV features appear in the western basin in the lee of Corsica–Sardinia (positive PV) and at the exit of the Ebro valley (Spain) where the cierzo blows. In the absence of nudging, the PV field is completely different from the PV field simulated with nudging, and is much more difficult to interpret, even though we still see the major PV banners associated with the mistral and tramontane, although they appear much narrower. The absence of nudging gives full freedom to the RCM at all spatial scales and the deviation of the RCM large-scale field from the GCM, affects considerably the small-scale field through complex nonlinear interactions.

PV fields in the simulations are decomposed into a large-scale part and a small-scale part by application of low-pass and high-pass Fourier filters with cut-off wavenumber $k_c = \pi/\Delta$, with $\Delta = 1.125°$ the ERA-40 resolution. Contrary to the ideal situation of section 2, we do not have a true reference solution q_{ref}, containing both large and small scales, to compare with. Our best approximation of reality is the ERA-40 reanalysis, containing only large scales. Concerning the small scales, we can compute their small-scale variability and compare their dependence on the nudging time τ with the prediction by the toy model. We

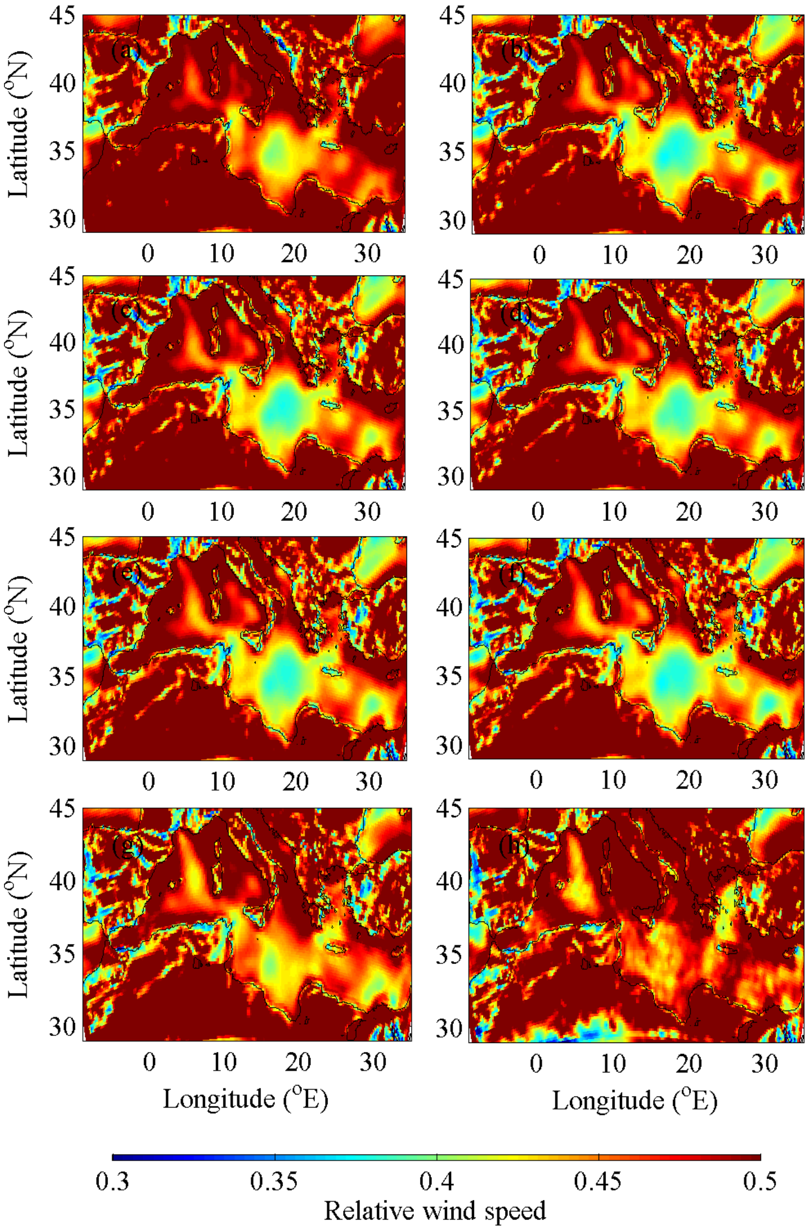

Figure 4. As Figure 3, but for the relative wind speed G. This figure is available in colour online at www.interscience.wiley.com/journal/qj

therefore focus on the τ dependance of:

$$\|q_r - q_{ref}\|_{ls}^2 = \int_{|k|<k_c} \left|\widehat{q}_r - \widehat{q}_{ref}\right|^2 d^2k, \quad (15)$$

$$\|q_r\|_{ss}^2 = \int_{|k|>k_c} \left|\widehat{q}_r\right|^2 d^2k. \quad (16)$$

According to section 2, these should behave as a function of τ as:

$$\|q_r - q_{ref}\|_{ls} \sim \|q_{ref}\|_{ls} \frac{\tau}{\tau_{num}}, \quad (17)$$

$$\|q_r\|_{ss} \sim \|q_{ref}\|_{ss} \left\{1 + \left(\frac{\tau_{ss}}{\tau}\right)^2\right\}^{-1/2}. \quad (18)$$

Equation (18) is analogous to Eq. (10) and can be derived the same way under the assumption $\tau_{num} \gg \tau_{ss}$.

We can actually go a bit further and derive a proxy expression for the small-scale error. Indeed comparing Eqs. (11) and (18) when $\tau \gg \tau_{ss}$ one finds that

$$\|q_r - q_{ref}\|_{ss}^2 \simeq \|q_{ref}\|_{ss}^2 - \|q_r\|_{ss}^2, \quad (19)$$

hence an estimate of the total (squared) error is

$$\epsilon_{tot}^2 = \epsilon_{ss}^2 + \epsilon_{ls}^2 \simeq \|q_{ref}\|_{ss}^2 + \|q_r - q_{ref}\|_{ls}^2 - \|q_r\|_{ss}^2. \quad (20)$$

Since $\|q_{ref}\|_{ss}^2$ is independent of τ, Eq. (20) expresses the fact that τ should be set short enough to keep $\|q_r - q_{ref}\|_{ls}^2$ small, and long enough to let the small-scale dynamics develop a significant $\|q_r\|_{ss}^2$. Looking for a minimum of $\|q_r - q_{ref}\|^2 - \|q_r\|_{ss}^2$ as a function of τ yields directly an estimate of τ_{opt}, bypassing the separate estimates of τ_{num} and τ_{ss}.

For a given day of the simulation, we compute $\|q_r - q_{ref}\|_{ls}$ and $\|q_r\|_{ss}$ for each MM5 simulation. The unknown value of $\|q_{ref}\|_{ss}$ is obtained as the value of $\|q_r\|_{ss}$

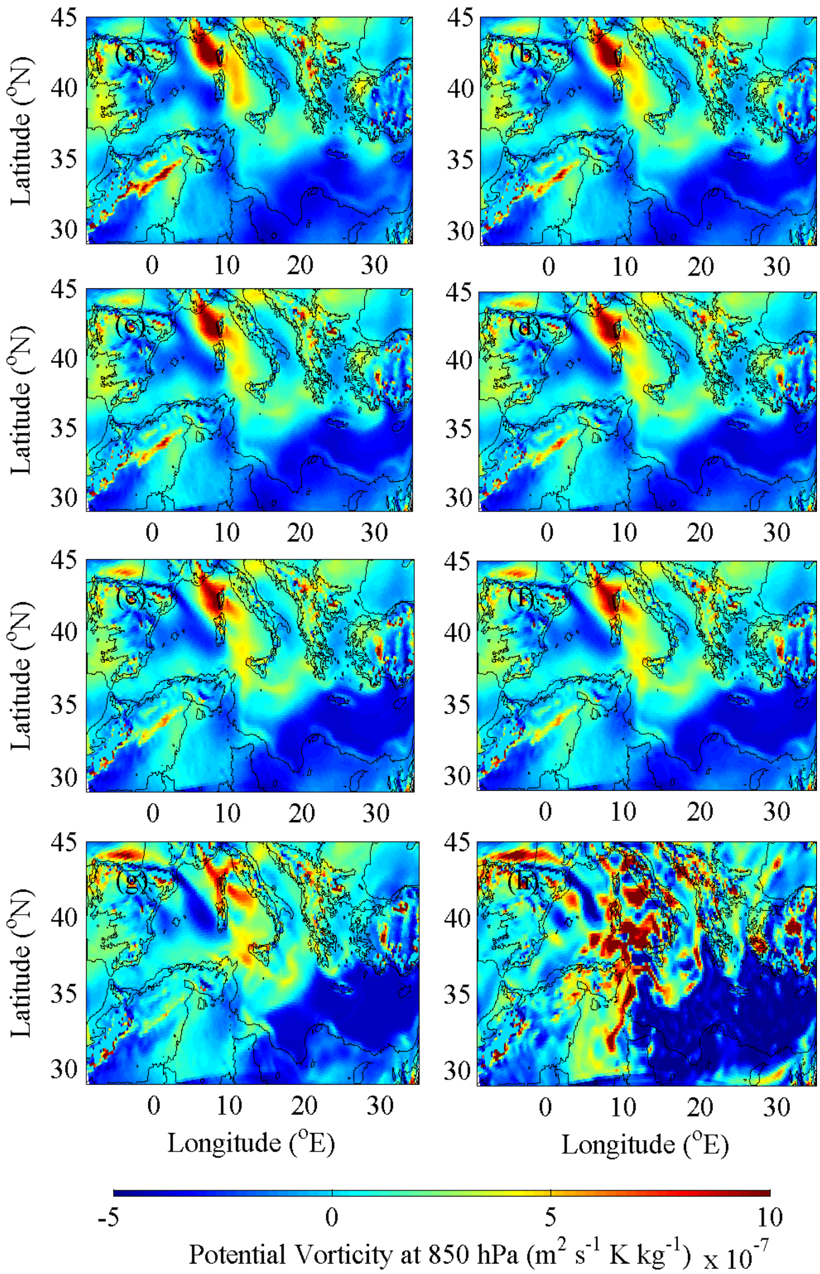

Figure 5. Potential vorticity at 850 hPa on day 20 of the MM5 RCM simulation at 0000 UTC for nudging time τ equal to (a) 1 h, (b) 2 h, (c) 3 h, (d) 4 h, (e) 5 h, (f) 6 h, (g) 12 h and (h) ∞ (no nudging). This figure is available in colour online at www.interscience.wiley.com/journal/qj

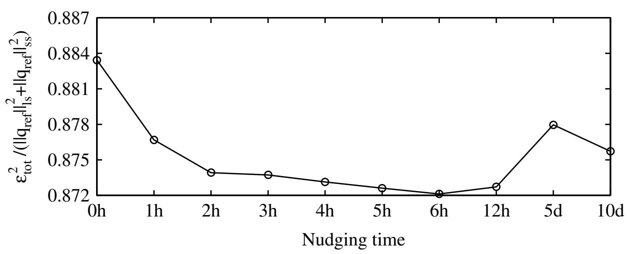

Figure 6. Normalized total error $\epsilon^2_{tot}/\left(\|q_{ref}\|^2_{ss} + \|q_{ref}\|^2_{ls}\right)$ computed from the MM5 RCM fields on day 20 of the simulation, as a function of τ.

in the simulation with $\tau = \infty$ (no nudging). Figure 6 shows the ϵ^2_{tot} normalized by $\|q_{ref}\|^2_{ss} + \|q_{ref}\|^2_{ls}$ as a function of τ.

A minimum (τ_{opt}) is reached for $\tau \sim 6$ h. However we have found when performing this analysis at other days in the simulations that the estimate of τ_{opt} is not very robust and subject to large variations. We therefore introduce a second estimate of τ_{opt} based not on the deviation of PV from a reference value but on the separate determination of τ_{num} and τ_{ss}. Going back to Eq. (17), one finds :

$$\|q_r\|_{ls} \sim \|q_{ref}\|_{ls}\left(1 + \frac{\tau}{\tau_{num}}\right)^{-1}. \tag{21}$$

Figure 7 displays the normalized quantities $\|\widehat{q}_r\|_{ls} / \|\widehat{q}_{ref}\|_{ls}$ and $\|\widehat{q}_r\|_{ss} / \|\widehat{q}_{ref}\|_{ss}$ as a function of τ.

Consistently with Eq. (17), $\|q_{ref}\|_{ls}$ is obtained from $\|q_r\|_{ls}$ for small τ. We now try and adjust the value of τ_{num} for $\|q_r\|_{ls} / \|q_{ref}\|_{ls}$ to match its theoretical expression $(1 + \tau/\tau_{num})^{-1}$ (Figure 6). For $0 \leq \tau \leq 1$ h, $\|q_r\|_{ls} / \|q_{ref}\|_{ls}$ decreases from 1 ($q = q_{ls}$) by about 5% (Figure 7(a)). This behaviour is systematic whatever the simulation day and is

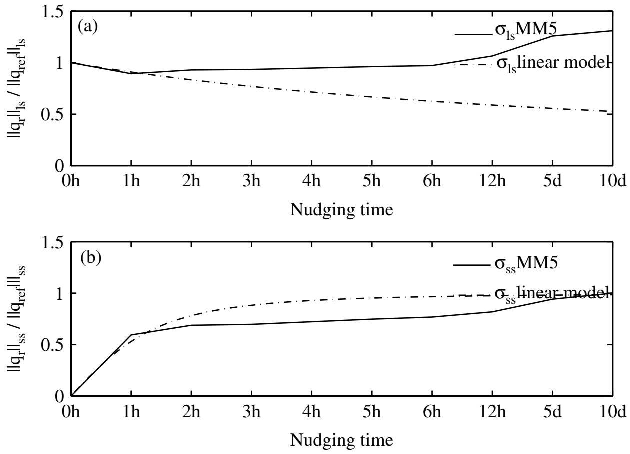

Figure 7. Normalized quantities (a) $\|\widehat{q}_r\|_{ls} / \|\widehat{q}_{ref}\|_{ls}$ and (b) $\|\widehat{q}_r\|_{ss} / \|\widehat{q}_{ref}\|_{ss}$ as a function of τ. The linear predictions given by Eqs. (21) and (18) (dash-dotted lines) are superimposed on those computed from the MM5 RCM fields (solid lines) on day 20 of the simulation.

consistent with Eq. (21), thus showing the effect of numerical diffusion which smooths the large-scale variability. For $1 < \tau < 12$ h, $\|q_r\|_{ls} / \|q_{ref}\|_{ls}$ remains nearly constant and increases for $\tau > 12$ h. Indeed, the linear model only allows the prediction of the contribution of numerical diffusion to the large-scale variability. The intrinsic limits of the linear model prevent the prediction of the contribution of the nonlinearities to the large-scale variability and the interactions between the large- and small-scale flows. In addition to these limits, our scale truncation into large and small scales leads to an estimation of $\|q_r\|_{ls} / \|q_{ref}\|_{ls}$ on a small number of points in the spectral domain, and probably a significant increase of the domain size (which however leads to a significant increase of the numerical cost) would have made more accurate the estimation of $\|q_r\|_{ls} / \|q_{ref}\|_{ls}$ (Seth and Giorgi, 1998). Approximating $\|q_r\|_{ls} / \|q_{ref}\|_{ls}$, Eq. (21) (dash-dotted line) gives $\tau_{num} \simeq 18$ h.

Figure 7 shows that $\|q_r\|_{ss} / \|q_{ref}\|_{ss}$ increases with τ to the asymptotic value of 1 for $\tau \geq 3$ h, approximately. The shape of the curve obtained from the MM5 RCM field is in very good agreement with the linear prediction and indicates that, even though the small-scale variability is most probably caused by nonlinear processes, the evolution of $\|q_r\|_{ss} / \|q_{ref}\|_{ss}$ with τ is well predicted by the linear expression given by Eq. (21). Approximating $\|q_r\|_{ss} / \|q_{ref}\|_{ss}$ with Eq. (21) (dash-dotted line), gives $\tau_{ss} \simeq 1.2$ h. Using Eq. (13), we obtain $\tau_{opt} \simeq 3.4$ h, which is close to the value obtained from the direct estimation (~ 6 h) and to the value chosen in many numerical studies which generally justify this choice by the time interval between consecutive analyzes or reanalyses used to drive the RCM (e.g. Salameh *et al.*, 2007; Champollion *et al.*, 2009).

In order to assess the significance of the τ_{opt} estimate, the estimation of τ_{num} and τ_{ss} is performed over the whole period of the simulation. Figure 8 displays τ_{num} and τ_{ss} computed every 5 d, as a function of the simulation day.

The estimation of τ_{num} seems to be not very robust since it results from the fitting of $\|q_r\|_{ls} / \|q_{ref}\|_{ls}$ with Eq. (21) on the first two nudging times only ($\tau \leq 1$ h), where the linear model matches best (e.g. Figure 7(a)). The estimation of τ_{ss} is more consistent from day to day. This is in agreement with the better fit in Figure 8(b).

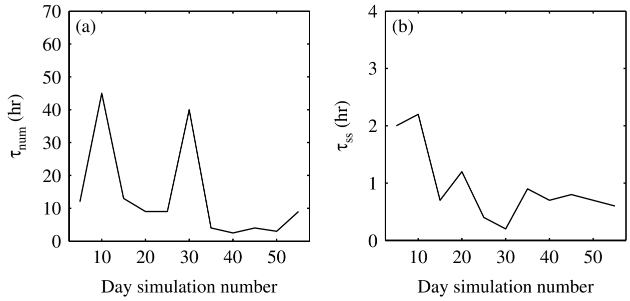

Figure 8. (a) τ_{num} and (b) τ_{ss}, as a function of the simulation day.

5. Conclusion

In this paper, a RCM is driven by the ERA-40 reanalyses produced by the ECMWF GCM to simulate the winter 1998 climate over the Mediterranean basin. We consider the effects on internal variability of temporal large-scale nudging which consists in relaxing the RCM's prognostic variables towards the GCM values within a predetermined relaxation time. A 'toy model', basically consisting of resolving a linear transport equation with a Newtonian relaxation term, predicts the existence of an optimal nudging time which depends on the time-scale over which numerical errors affect significantly the accuracy of the 'regional' solution at the large spatial scales, and the typical time-scale of the small-scale phenomena that are not resolved by the GCM.

The comparison between the RCM and the prediction of the linear model evidences the limits of this model, especially when the large-scale field is considered. Indeed, the linear model only allows the prediction of the contribution of numerical diffusion to the large-scale variability, but not the contribution of the nonlinearities to the large-scale variability and the interactions between the large- and small-scale flows. Despite, this limitation, the comparison between the RCM and the linear model allows the prediction of a reasonable optimal nudging time that is close to the value commonly used and usually chosen based on trial and error or non-dynamical arguments.

An important feature of our toy model is the absence of nonlinearities. This simplicity allowed an analytic treatment of the problem and we identified the competing time-scales which control the discrepancy between the regional simulation and the ideal flow state. One time-scale is set by the small-scale dynamics and controls small-scale error. The other time-scale controls large-scale errors, due to the 'regional model' drifting away from the 'reanalyses', and is set in our toy model by numerical dissipation. However it is apparent in Figure 7 that our estimate of the latter time-scale in a realistic model is disputable since large-scale variance increases as the nudging time is increased, unlike our estimate (Eq. 21). It is plausible that this increase reflects a feedback of the small scales, which develop for long nudging times, onto the large scales. This possibility is ruled out in our model because of its linearity. Hence Eq. (13) should not be considered as a generally valid prescription of an ideal nudging time, but instead as a stimulus to identify the two problem-dependent time-scales τ_{ss} and τ_{num}. For instance, in a realistic, nonlinear model, the drift of the regional simulation away from the reanalyses may not be caused mainly by numerical errors but rather by an intrinsic lack of predictability, which is usually attributed to the nonlinear feedback of small scales onto large scales. Future work should assess this hypothesis in fully nonlinear models of intermediate complexity, such as geostrophic turbulence, in order to provide additional, dynamically based guidance on the choice of appropriate nudging times.

Acknowledgement

We are thankful to the three anonymous referees who helped to improve the manuscript significantly. This research has received funding from the Agence de l'Environnement et de la Maîtrise de l'Énergie (ADEME). This work was also supported by ANR-MEDUP and GIS 'Climat-Environnement-Société' MORCE-MED projects.

Appendix

Error estimate

In order to estimate the effect of the nudging time on the errors made at large and small scales, we analyze Eq. (6) in Fourier space:

$$\begin{aligned} q_{\mathrm{ls}}(x,t) &= \int \widehat{q}_{\mathrm{ls}}(k,t)\mathrm{e}^{\mathrm{i}kx}\,\mathrm{d}k\,, \\ q_{\mathrm{ss}}(x,t) &= \int \widehat{q}_{\mathrm{ss}}(k,t)\mathrm{e}^{\mathrm{i}kx}\,\mathrm{d}k\,, \end{aligned} \tag{A.1}$$

where k is the wave number. Eq. (6) then becomes:

$$\frac{\partial \widehat{q}_{\mathrm{r}}}{\partial t} + \widehat{q}_{\mathrm{r}}\left(\mathrm{i}k\overline{U} + \frac{1}{\tau} + K_{\mathrm{num}}k^2\right) = \mathrm{i}k\overline{U}\widehat{q}_{\mathrm{ss}} + \frac{1}{\tau}\widehat{q}_0\mathrm{e}^{-\mathrm{i}k\overline{U}t}. \tag{A.2}$$

The solution of this equation is the sum of a homogeneous solution without the right-hand side and a particular solution for the right-hand side. The homogenous solution is $\widehat{q}_{\mathrm{hom}} = Cst\,\mathrm{e}^{-At}$, where Cst is a constant and $A = \mathrm{i}k\overline{U} + \tau^{-1} + K_{\mathrm{num}}k^2$. We find a particular solution of Eq. (A.2) of the form $C(t)\mathrm{e}^{-At}$ where

$$C(t) = \mathrm{i}k\overline{U}q_{\mathrm{ss}}\frac{\mathrm{e}^{At}}{A} + \frac{1}{\tau}\widehat{q}_{\mathrm{ls}}\frac{\mathrm{e}^{At}}{A - \mathrm{i}k\overline{U}}\,, \tag{A.3}$$

with $\widehat{q}_{\mathrm{ls}} = \widehat{q}_0\mathrm{e}^{-\mathrm{i}k\overline{U}t}$. The general solution of Eq. (A.2) (hereafter called regional solution $\widehat{q}_{\mathrm{r}}$) is then finally:

$$\begin{aligned} \widehat{q}_{\mathrm{r}}(k,t) = \widehat{q}_{\mathrm{ls}}(k,t)&\frac{1}{1 + K_{\mathrm{num}}k^2\tau} \\ + \widehat{q}_{\mathrm{ss}}(k)&\frac{\mathrm{i}\overline{U}k}{\mathrm{i}k\overline{U} + \tau^{-1} + K_{\mathrm{num}}k^2}\,, \end{aligned} \tag{A.4}$$

which differs from the ideal solution (obtained when $\tau = \infty$ and $K_{\mathrm{num}} = 0$) by:

$$\begin{aligned} \widehat{q}_{\mathrm{r}}(k,t) &- \widehat{q}_{\mathrm{ls}}(k,t) - \widehat{q}_{\mathrm{ss}}(k) \\ &= \widehat{q}_{\mathrm{ls}}(k,t)\left(\frac{1}{1 + K_{\mathrm{num}}k^2\tau} - 1\right) \\ &+ \widehat{q}_{\mathrm{ss}}(k)\left(\frac{\mathrm{i}\overline{U}k}{\mathrm{i}k\overline{U} + \tau^{-1} + K_{\mathrm{num}}k^2} - 1\right). \end{aligned} \tag{A.5}$$

Hence the error present in the regional solution q_{r} can be decomposed into a large-scale contribution proportional to q_{ls} and a small-scale contribution proportional to q_{ss}. This provides a bound on the r.m.s error ϵ:

$$\epsilon \le \epsilon_{\mathrm{ls}} + \epsilon_{\mathrm{ss}}\,, \tag{A.6}$$

where

$$\left\|\widehat{q}(k)\right\| = \left(\int \left|\widehat{q}(k)\right|^2 \mathrm{d}k\right)^{1/2}, \tag{A.7}$$

$$\begin{aligned} \epsilon &= \left\|\widehat{q}_{\mathrm{r}}(k,t) - \widehat{q}_{\mathrm{ls}}(k,t) - \widehat{q}_{\mathrm{ss}}(k)\right\|\,, \\ \epsilon_{\mathrm{ls}} &= \left\|\widehat{q}_{\mathrm{ls}}(k,t)\left(\frac{1}{1 + K_{\mathrm{num}}k^2\tau} - 1\right)\right\|\,, \\ \epsilon_{\mathrm{ss}} &= \left\|\widehat{q}_{\mathrm{ss}}(k)\left(\frac{\mathrm{i}k\overline{U}}{\mathrm{i}k\overline{U} + \frac{1}{\tau} + K_{\mathrm{num}}k^2} - 1\right)\right\|. \end{aligned} \tag{A.8}$$

We shall consider $\epsilon_{\mathrm{ls}} + \epsilon_{\mathrm{ss}}$ as our best estimate of the r.m.s. error, and as the quantity to be minimized as a function of the nudging time τ. Given characteristic scales $L_{\mathrm{ls}} \gg L_{\mathrm{ss}}$, corresponding to wave numbers $k_{\mathrm{ls}} \ll k_{\mathrm{ss}}$, of the functions q_{ls} and q_{ss}, we obtain the estimates

$$\begin{aligned} \epsilon_{\mathrm{ls}} &\sim \left\|\widehat{q}_{\mathrm{ls}}\right\|\left|\frac{1}{1 + K_{\mathrm{num}}k_{\mathrm{ls}}^2\tau} - 1\right|, \\ \epsilon_{\mathrm{ss}} &\sim \left\|\widehat{q}_{\mathrm{ss}}\right\|\left|\frac{1}{1 - \mathrm{i}\left(\tau\overline{U}k_{\mathrm{ss}}\right)^{-1} - \mathrm{i}K_{\mathrm{num}}k_{\mathrm{ss}}/\overline{U}} - 1\right| \\ &\sim \left\|\widehat{q}_{\mathrm{ss}}\right\|\left|\frac{1}{1 + \left(\mathrm{i}\tau\overline{U}k_{\mathrm{ss}}\right)^{-1}} - 1\right|. \end{aligned} \tag{A.9}$$

The last approximation stems from the fact that, for low-order time and space discretizations, the numerical diffusion is typically $K_{\mathrm{num}} \sim \overline{U}^2\Delta t$; furthermore, the time step Δt is usually limited by the Courant–Friedrich–Levy stability condition $\overline{U}\Delta t \le \Delta x$ where Δx is the spatial grid resolution. In that case $K_{\mathrm{num}}k_{\mathrm{ss}}/\overline{U} \sim \overline{U}k_{\mathrm{ss}}\Delta t < k_{\mathrm{ss}}\Delta x < \pi$ while, as we shall see, the optimal nudging time is such that $\left(\tau\overline{U}k_{\mathrm{ss}}\right)^{-1} \gg 1$.

References

Aebischer U, Schär C. 1998. Low-level potential vorticity and cyclogenesis to the lee of the Alps. *J. Atmos. Sci.* **55**: 186–207.

Bhaskaran B, Jones RG, Murphy JM, Noguer M. 1996. Simulations of the Indian summer monsoon using a nested regional climate model: Domain size experiments. *Clim. Dyn.* **12**: 573–587.

Caccia JL, Guénard V, Bénech B, Campistron B, Drobinski P. 2004. Vertical velocity and turbulence aspects during mistral events as observed by UHF wind profilers. *Ann. Geophys.* **22**: 3927–3936.

Champollion C, Drobinski P, Haeffelin M, Bock O, Tarniewicz J, Bouin MN, Vautard R. 2009. Water vapour variability induced by urban/rural heterogeneities during convective conditions. *Q. J. R. Meteorol. Soc.* **135**: 1266–1276.

Chen F, Dudhia J. 2001. Coupling and advanced land surface-hydrology model with the Penn State-NCAR MM5 modeling system. Part I: Model implementation and sensitivity. *Mon. Weather Rev.* **129**: 569–585.

Corsmeier U, Behrendt R, Drobinski P, Kottmeier C. 2005. The mistral and its effect on air pollution transport and vertical mixing. *Atmos. Res.* **74**: 275–302.

Davies HC, Turner RE. 1977. Updating prediction models by dynamical relaxation: An examination of the technique. *Q. J. R. Meteorol. Soc.* **103**: 225–245.

Denis B, Laprise R, Caya D, Côté J. 2002. Downscaling ability of one-way nested regional climate models: The Big-Brother Experiment. *Clim. Dyn.* **18**: 627–646.

Denis B, Laprise R, Caya D. 2003. Sensitivity of a regional climate model to the resolution of the lateral boundary conditions. *Clim. Dyn.* **20**: 107–126.

Drobinski P, Flamant C, Dusek J, Flamant PH, Pelon J. 2001. Observational evidence and modeling of an internal hydraulic jump at the atmospheric boundary-layer top during a tramontane event. *Boundary-Layer Meteorol.* **98**: 497–515.

Drobinski P, Bastin S, Guénard V, Caccia JL, Dabas AM, Delville P, Protat A, Reitebuch O, Werner C. 2005. Summer mistral at the exit of the Rhône valley. *Q. J. R. Meteorol. Soc.* **131**: 353–375.

Dudhia J. 1993. A nonhydrostatic version of the Penn State/NCAR mesoscale model: Validation tests and simulations of an Atlantic cyclone and cold front. *Mon. Weather Rev.* **121**: 1493–1513. Mon. Wea. Rev., 121, 1493–1513.

Dünkeloh A, Jacobeit J. 2003. Circulation dynamics of Mediterranean precipitation variability 1948–1998. *Int. J. Climatol.* **23**: 1843–1866.

Efimov V, Shokurov M. 2002. Spatiotemporal structure of the surface wind field over the Black Sea. *Izv. Acad. Sci. USSR, Atmos. Oceanic Phys.* **38**: 421–430.

Flamant C, Richard E, Schär C, Rotunno R, Nance L, Sprenger M, Benoit R. 2004. The wake south of the Alps: Dynamics and structure of the lee-side flow and secondary potential vorticity banners. *Q. J. R. Meteorol. Soc.* **130**: 1275–1303.

Genthon C, Krinner G, Cosme E. 2002. Free and laterally nudged Antartic climate of an atmospheric general circulation model. *Mon. Weather Rev.* **130**: 1601–1616.

Giorgi F. 1990. Simulation of regional climate using a limited-area model nested in a general circulation model. *J. Climate* **3**: 941–963.

Grell GA. 1993. Prognostic evaluation of assumptions used by cumulus parametrizations. *Mon. Weather Rev.* **121**: 764–787.

Grell GA, Dudhia J, Stauffer DR. 1993. '*A description of the fifth-generation Penn State/NCAR mesoscale model (MM5)*'. Technical Note NCAR/TN-398+STR. NCAR: Boulder, CO, USA.

Guénard V, Drobinski P, Caccia JL, Campistron B, Bénech B. 2005. An observational study of the mesoscale mistral dynamics. *Boundary-Layer Meteorol.* **115**: 263–288.

Guénard V, Drobinski P, Caccia JL, Tedeschi G, Currier P. 2006. Dynamics of the MAP IOP-15 severe mistral event: Observations and high-resolution numerical simulations. *Q. J. R. Meteorol. Soc.* **132**: 757–778.

Guo YR, Chen S. 1994. '*Terrain and land use for the fifth-generation Penn State/NCAR mesoscale modeling system (MM5)*'. Technical Note NCAR/TN-397+IA. NCAR: Boulder, CO, USA.

Hong SY, Pan HL. 1996. Nonlocal boundary layer vertical diffusion in a medium-range forecast model. *Mon. Weather Rev.* **124**: 2322–2339.

Jansá A. 1987. Distribution of the mistral: A satellite observation. *Meteorol. Atmos. Phys.* **36**: 201–214.

Jiang Q, Smith RB, Doyle J. 2003. The nature of the mistral: Observations and modelling of two MAP events. *Q. J. R. Meteorol. Soc.* **129**: 857–876.

Jurčec V. 1981. On mesoscale characteristics of bora conditions in Yugoslavia. *Pure Appl. Geophys.* **199**: 640–657.

Lafore JP, Stein J, Asencio N, Bougeault P, Ducrocq V, Duron J, Fischer C, Héreil P, Mascart P, Masson V, Pinty JP, Redelsperger JL, Richard E, Vilà-Guerau de Arellano J. 1998. The Méso-NH atmospheric simulation system. Part I: Adiabatic formulation and control simulation. *Ann. Geophys.* **16**: 90–109.

Laprise R, Varma MR, Denis B, Caya D, Zawadzki I. 2000. Predictibility of a nested limited-area model. *Mon. Weather Rev.* **128**: 4149–4154.

Lebeaupin Brossier C, Drobinski P. 2009. Numerical high-resolution air-sea coupling over the Gulf of Lions during two tramontane/mistral events. *J. Geophys. Res.* **114**: D10110, DOI: 10.1029/2008JD011601

Li Y, Ménard R, Riishojgaard LP, Cohn SE, Rood RB. 1998. A study on assimilating potential vorticity data. *Tellus A* **50**: 490–506.

Lo JCF, Yang ZL, Pielke RA Sr. 2008. Assessment of three dynamical climate downscaling methods using the Weather Research and Forecasting (WRF) model. *J. Geophys. Res.* **113**: D09112, DOI: 10.1029/2007JD009216

Mariotti A, Struglia MV, Zeng N, Lau KM. 2002. The hydrological cycle in the Mediterranean region and implications for the water budget of the Mediterranean Sea. *J. Climate* **15**: 1674–1690.

Mass FC, Ovens D, Westrick K, Colle BA. 2002. Does increasing horizontal resolution produce more skillful forecast? *Bull. Am. Meteorol. Soc.* **83**: 407–430.

Mlawer EJ, Taubman SJ, Brown PD, Iacono MJ, Clough SA. 1997. Radiative transfer for inhomogeneous atmosphere: RRTM, a validated correlated-k model for the longwave. *J. Geophys. Res.* **102**(D14): 16663–16682.

Noguer M, Jones R, Murphy J. 1998. Sources of systematic errors in the climatology of a regional climate model over Europe. *Clim. Dyn.* **14**: 691–712.

Pandžic K, Likso T. 2005. Eastern Adriatic typical wind field patterns and large-scale atmospheric conditions. *Int. J. Climatol.* **25**: 81–98.

Pielke RA, Cotton WR, Walko RL, Tremback CJ, Nicholls ME, Moran MD, Wesley DA, Lee TJ, Copeland JH. 1992. A comprehensive meteorological modeling system RAMS. *Meteorol. Atmos. Phys.* **49**: 69–91.

Price C, Stone L, Rajagopalan B, Alpert P. 1998. A possible link between El Niño and precipitation in Israel. *Geophys. Res. Lett.* **25**: 3963–3966.

Qian JH, Seth A, Zebiak S. 2003. Reinitialized versus continuous simulations for regional climate downscaling. *Mon. Weather Rev.* **131**: 2857–2874.

Reale O, Feudale L, Turato B. 2001. Evaporative moisture sources during a sequence of floods in the Mediterranean region. *Geophys. Res. Lett.* **28**: 2085–2088.

Reisner J, Rasmussen RJ, Bruintjes RT. 1998. Explicit forecasting of supercooled liquid water in winter storms using the MM5 mesoscale model. *Q. J. R. Meteorol. Soc.* **124**: 1071–1107.

Rodó X. 2001. Reversal of three global atmospheric fields linking changes in SST anomalies in the Pacific, Atlantic and Indian Oceans at tropical latitudes and midlatitudes. *Clim. Dyn.* **18**: 203–217.

Rodó X, Baert E, Comín FA. 1997. Variations in seasonal rainfall in Southern Europe during the present century: Relationships with the North Atlantic Oscillation and the El Niño–Southern Oscillation. *Clim. Dyn.* **13**: 275–284.

Rodriguez-Fonseca B, De Castro M. 2002. On the connection between winter anomalous precipitation in the Iberian Peninsula and North West Africa and the summer subtropical Atlantic sea surface temperature. *Geophys. Res. Lett.* **29**: DOI: 10.1029/2001GL014421

Rodwell MJ, Hoskins BJ. 1996. Monsoons and the dynamics of deserts. *Q. J. R. Meteorol. Soc.* **122**: 1385–1404.

Salameh T, Drobinski P, Menut L, Bessagnet B, Flamant C, Hodzic A, Vautard R. 2007. Aerosol distribution over the western Mediterranean basin during a tramontane/mistral event. *Ann. Geophys.* **11**: 2271–2291.

Salameh T, Drobinski P, Vrac M, Naveau P. 2009. Statistical downscaling of near-surface wind over complex terrain in southern France. *Meteorol. Atmos. Phys.* **103**: 243–256.

Schär C, Sprenger M, Luthi D, Jiang QF, Smith RB, Benoit R. 2003. Structure and dynamics of an Alpine potential vorticity banner. *Q. J. R. Meteorol. Soc.* **129**: 825–855.

Schraff CH. 1997. Mesoscale data assimilation and prediction of low stratus in the Alpine region. *Meteorol. Atmos. Phys.* **64**: 21–50.

Seth A, Giorgi F. 1998. The effects of domain choice on summer precipitation simulation and sensitivity in a regional climate model. *J. Climate* **11**: 2698–2712.

Skamarock WC, Klemp JB, Dudhiav, Gill DO, Barker DM, Wang W, Powers JG. 2005. '*A Description of the Advanced Research WRF Version 2*'. Technical Note NCAR/TN-468+STR. NCAR: Boulder, CO, USA.

Smith RB. 1987. Aerial observations of the Yugoslavian bora. *J. Atmos. Sci.* **44**: 269–297.

Smith RB. 1989. Mountain-induced stagnation points in hydrostatic flow. *Tellus A* **41**: 270–274.

Smith RB, Doyle JD, Jiang Q, Smith S. 2007. Alpine gravity waves: Lessons from MAP regarding mountain wave generation and breaking. *Q. J. R. Meteorol. Soc.* **133**: 914–936.

Trigo RM, Trigo IF, DaCamara C, Osborn TJ. 2004. Climate impact on the European winter blocking episodes from the NCEP/NCAR reanalyses. *Clim. Dyn.* **23**: 17–28.

Vidard PA, Le Dimet FX, Piacentini A. 2003. Determination of optimal nudging coefficients. *Tellus A* **55**: 1–15.

Von Storch H, Langenberg H, Feser F. 2000. A spectral nudging technique for dynamical downscaling purposes. *Mon. Weather Rev.* **128**: 3664–3673.

Waldron KM, Paegle J, Horel JD. 1996. Sensitivity of a spectrally filtered and nudged limited-area model to outer model options. *Mon. Weather Rev.* **124**: 529–547.

Wilby RL, Wigley TML. 1997. Downscaling general circulation model output: A review of methods and limitations. *Prog. Phys. Geog.* **21**: 530–548.

Wilby RL, Wigley TML, Conway D, Jones PD, Hewitson BC, Main J, Wilks DS. 1998. Statistical downscaling of general circulation model output: A comparison of methods. *Water Resour. Res.* **34**: 2995–3008.

Xoplaki E. 2002. 'Climate variability over the Mediterranean'. PhD thesis, University of Bern, Switzerland.

Yoshino MM, Yoshino MT, Yoshimura M, Mitsui K, Urushibara K, Ueda S, Owada M, Nakamra K. 1976. Bora regions as revealed by wind-shaped trees on the Adriatic Coast. In *Local Wind Bora*. Yoshino MM (ed.) University of Tokyo Press: Tokyo, Japan. 59–71.

Žagar N, Žagar M, Cedilnik J, Gregorič G, Rakovec J. 2006. Validation of mesoscale low-level winds obtained by dynamical downscaling of ERA-40 over complex terrain. *Tellus A* **58**: 445–455.
Zecchetto S, De Biasio F. 2006. Sea surface winds over the Mediterranean basin from satellite data (2000–04): Meso- and local-scale features on annual and seasonal time scales. *J. Appl. Meteorol. Climatol.* **46**: 814–827.
Ziv B, Saaroni H, Alpert P. 2004. The factors governing the summer regime of the eastern Mediterranean. *Int. J. Climatol.* **24**: 1859–1871.

